

Article

Well-Dispersed CoNiO₂ Nanosheet/CoNi Nanocrystal Arrays Anchored onto Monolayer MXene for Superior Electromagnetic Absorption at Low Frequencies

LeiYu Du ¹, Renxin Xu ^{1,*}, Yunfa Si ¹, Wei Zhao ¹, Hongyi Luo ¹, Wei Jin ² and Dan Liu ^{3,4,*} 

- ¹ School of Materials Science and Engineering, Wuhan University of Technology, 122 Luoshi Road, Wuhan 430070, China; duleiyv@whut.edu.cn (L.D.); siyunfa@whut.edu.cn (Y.S.); zw0712@163.com (W.Z.); luohongyi@whut.edu.cn (H.L.)
- ² State Key Laboratory of Silicate Materials for Architectures, Wuhan University of Technology, 122 Luoshi Road, Wuhan 430070, China; jinwei@whut.edu.cn
- ³ Department of Chemistry, School of Chemistry, Chemical Engineering and Life Sciences, Wuhan University of Technology, 122 Luoshi Road, Wuhan 430070, China
- ⁴ Foshan Xianhu Laboratory of the Advanced Energy Science and Technology Guangdong Laboratory, Xianhu Hydrogen Valley, 1 Yangming Road, Foshan 528200, China
- * Correspondence: xurenxin@whut.edu.cn (R.X.); danielliu@whut.edu.cn (D.L.)

Abstract: Developing microwave absorbers with superior low-frequency electromagnetic wave absorption properties is one of the foremost important factors driving the boom in 5G technology development. In this study, via a simple hydrothermal and pyrolysis strategy, randomly interleaved CoNiO₂ nanosheets and uniformly ultrafine CoNi nanocrystals are anchored onto both sides of a single-layered MXene. The absorption mechanism demonstrated that the hierarchical heterostructure prevents the aggregation of MXene nanoflakes and magnetic crystallites. In addition, the introduction of the double-magnetic phase of CoNiO₂/CoNi arrays can not only enhance the magnetic loss capacity but also generate larger void spaces and abundant heterogeneous interfaces, collectively promoting impedance-matching and furthering microwave attenuation capabilities at a low frequency. Hence, the reflection loss of the optimal absorber (M-MCNO) is −45.33 dB at 3.24 GHz, which corresponds to a matching thickness of 5.0 mm. Moreover, its EAB can entirely cover the S-band and C-band by tailoring the matching thickness from 2 to 7 mm. Satellite radar cross-section (RCS) simulations demonstrated that the M-MCNO can reduce the RCS value to below −10 dB m² over a multi-angle range. Thus, the proposed hybrid absorber is of great significance for the development of magnetized MXene composites with superior low-frequency microwave absorption properties.

Keywords: MXene; magnetic nanosheet; magnetic nanocrystal; hierarchical heterostructure; low-frequency absorption



Citation: Du, L.; Xu, R.; Si, Y.; Zhao, W.; Luo, H.; Jin, W.; Liu, D. Well-Dispersed CoNiO₂ Nanosheet/CoNi Nanocrystal Arrays Anchored onto Monolayer MXene for Superior Electromagnetic Absorption at Low Frequencies. *Coatings* **2024**, *14*, 631. <https://doi.org/10.3390/coatings14050631>

Academic Editor: Chang Kwon Hwangbo

Received: 13 April 2024

Revised: 6 May 2024

Accepted: 9 May 2024

Published: 16 May 2024



Copyright: © 2024 by the authors. Licensee MDPI, Basel, Switzerland. This article is an open access article distributed under the terms and conditions of the Creative Commons Attribution (CC BY) license (<https://creativecommons.org/licenses/by/4.0/>).

1. Introduction

Recently, with the flourishing advancement of 5G communication technology, electromagnetic (EM) pollution has increasingly attracted people's attention due to its negative impact on human health and surrounding electronic devices [1]. To effectively address this issue, many measures have been taken to develop emerging low-frequency microwave absorbing materials (MAMs) such as magnetic loss absorbers [2–5], dielectric loss absorbers [6–8], and their composites [9–12]. Among these, MXene in particular, with its two-dimensional (2D) architecture, plays a vital role in high-performance low-frequency MAMs thanks to its superior conductive loss and impressive polarization loss rooting from abundant surface groups (e.g., -H, -F and -OH) [13]. For instance, the reflection loss (RL) of TiO₂@MXene composites in the S-band and C-band is less than −10 dB [6]. MXene aerogel delivers a minimum reflection loss (RL_{min}) of −41.8 dB at 5.8 GHz [7]. However, owing to the excessive permittivity and negligible permeability, serious impedance mismatch

in these highly conductive materials triggers off EM wave reflecting on the surface of an absorber rather than penetrating into the interior to be effectively attenuated, which significantly lowers the microwave absorption capacity [14]. Therefore, developing low-frequency MXene-based MAMs featuring perfect impedance-matching is a great responsibility and a significant challenge.

It is known that impedance-matching is dominated by the complex permeability (μ_r) and complex permittivity (ϵ_r) in MAMs. Namely, the normalized input impedance of an absorber can be tailored by improving its complex permeability as well as by decreasing its complex permittivity [15]. Thus, embedding magnetic components in MXene nanoflakes to form hybrids with dual magnetic/dielectric loss mechanisms is an efficient strategy to balance the two EM parameters. For example, Fe@MXene composite, fabricated by a template method, demonstrates an RL of -40.3 dB at 4.78 GHz [16]. The Ni@MXene hybrid, prepared via a solvothermal method, represents an RL_{\min} of -40.9 dB at 3.9 GHz [17]. Nevertheless, due to Snoek's limit, the low-frequency permeability of magnetized MXene nanoflakes is usually far lower than their permittivity even in the composites with extremely high magnetic phase dosage [9]. Additionally, owing to the magnetic dipole–dipole attractions and high surface energies, magnetic nanomaterials are liable to agglomeration as the loading contents rise, which can obviously improve the conductivity of a hybrid [10]. As a result, it is difficult to achieve impressive impedance-matching only by increasing the ratio of magnetic components in composites. Fortunately, apart from the intrinsic characteristics of a magnet, the geometric shape and size of magnetic nanocrystal can significantly affect the low-frequency permeability of a MAM. In other words, magnetic nanosheets with high aspect ratios can be conducive to generate significant magnetocrystalline anisotropy, when it is beneficial to exceed Snoek's limit in the gigahertz frequency range [18]. Furthermore, downsizing magnetic nanoparticles to nanoscale can enhance the inter-crystalline magnetic coupling, thereby boosting magnetocrystalline anisotropy at a low frequency [19]. Hence, based on the above considerations, to perfect impedance-matching and enhance the microwave attenuation ability at low frequency, an effective strategy is to construct magnetic nanosheets and/or ultrafine magnetic nanoparticles decorating on the surfaces of MXene nanoflakes.

In our work, we developed a novel strategy to prepare the single-layered MXene nanoflakes simultaneously loaded with randomly interlaced CoNiO₂ nanosheets and uniformly ultrafine CoNi nanocrystals via hydrothermal and calcination procedures. The system mechanism study showcases that the simultaneous in situ generation of interleaved cobalt and nickel hydrates nanosheets occurred on the surface of negatively charged MXene nanoflakes under the controlled low supersaturation and weakly alkaline environment. During the subsequent pyrolysis in Ar atmosphere, Co/Ni hydrate nanosheets were pyrolyzed to randomly interlocked CoNiO₂ nanosheets and uniformly ultrafine CoNi nanograins, implanting onto both surfaces of MXene nanoflakes. The obtained well-dispersed magnetic nanosheets and nanoparticles significantly further the permeability of the composite absorber, which is conducive to perfecting impedance matching. Moreover, the hierarchical network structures and multi-heterogeneous interfaces in these magnetized MXene nanoflakes can synergistically promote conduction loss, interfacial polarization, and dipolar polarization, boosting the microwave attenuation capacity. As anticipated, the CoNiO₂ nanosheets and CoNi nanoparticles jointly decorating MXene nanoflakes demonstrate the distinguished EM absorbing properties at low frequency. This study presents an efficient and versatile approach for designing high-performance low-frequency MXene-based MAMs.

2. Materials and Methods

2.1. Chemical Reagent

Ti₃AlC₂ MAX powders (400 mesh) were provided by Jilin 11 Technology Co., Jilin, China. Hydrochloric acid (HCl), lithium fluoride (LiF), nickel nitrate hexahydrate, and cobalt nitrate hexahydrate (Co(NO₃)₂·6H₂O) were obtained from Aladdin Shanghai Biological Technology Co, Ltd., Shanghai, China. Hexamethylenetetramine (HMT, C₆H₁₂N₄) and

anhydrous ethanol were brought from Sinopharm Chemical Reagent Co., Shanghai, China. All reagents were analytically pure.

2.2. Preparation of Monolayer MXene Nanoflakes

In a universal synthesis process [20], 1.0 g Ti_3AlC_2 powders were slowly added into a mixture with 16 mL hydrochloric acid, 4 mL deionized water, and 1.6 g LiF, continuously stirring at 50 °C for 30 h in a water bath. Then, the resulting solution was thoroughly washed with deionized water by centrifugation (3500 rpm) until self-delamination occurred at the supernatant pH of ~6. After that, the obtained centrifuging dark green supernatant was centrifuged at 5000 rpm for 0.5 h. Then, the sediment containing abundant monolayer MXene flakes was gathered. Finally, the resultant monolayer MXene nanoflakes were obtained by freeze-drying.

2.3. Preparation of $\text{CoNiO}_2/\text{CoNi}$ Co-Decorating MXene

A total of 100 mg monolayered MXene nanoflakes were added into absolute ethanol and further ultrasonicated until completely dispersed, while 2 mmol $\text{Co}(\text{NO}_3)_2 \cdot 6\text{H}_2\text{O}$ and 2 mmol $\text{Ni}(\text{NO}_3)_2 \cdot 6\text{H}_2\text{O}$ were added into absolute ethanol and magnetic-stirred until completely dissolved. Next, the above metal salt solution was dropped into the MXene solution and stirred to form a 20 mL mixture. Afterward, 6 mmol of HMT was added into the homogenous solution, which was then moved to a 50 mL Teflon-lined stainless-steel autoclave. After keeping at 120 °C for 5 h, the precipitation was harvested by repeatedly washing with deionized water and ethanol and then dried at 100 °C by a vacuum device for 12 h. Finally, the precursor powders were pyrolyzed in an Ar atmosphere at 500 °C for 1 h at a rate of 4 °C/min to gain the resulting single-layered MXene co-decorated with CoNiO_2 nanosheets and CoNi nanocrystals, named M-MCNO. In order to optimize the dielectric–magnetic ratio and hierarchical structure, other magnetized MXene-based composites with different dosages of MXene nanoflakes (0 mg, 50 mg, 200 mg) denoted as CNO, L-MCNO and H-MCNO were prepared by the same procedures. For comparison, another control MXene-based sample (labeled as MXene/CNO) was prepared by physically mixing pure MXene nanoflakes with CNO in an aqueous solution and then vacuum drying at 100 °C for 12 h.

2.4. Material Characterization

The micromorphology was investigated by scanning electron microscopy (SEM, ZEISS Gemini SEM 300). The nanoarchitecture was determined by transmission electron microscopy (TEM, FEI USA Talos F200X) and X-ray energy dispersive spectrometry (EDS). The crystal phase analysis was identified by X-ray diffraction (XRD, Bruker, Germany, D8 Advance) operating with a $\text{Cu K}\alpha$ source ($\lambda = 1.5418 \text{ \AA}$). The sample's surface binding energies were investigated using X-ray photoelectron spectroscopy spectra (XPS, Thermo ESCALAB China 250Xi) with an Al-K α X-ray source. The thermal stability was investigated using thermogravimetric (TG, NETZSCH Gemini STA449F3) analysis under argon. The composites' magnetization measurements were tested with vibrating sample magnetometer (VSM, KES USA Lakeshore 7404).

The EM parameters were performed by a vector network analyzer (PNA-N5244A, AGILENT China E5071C) at the range of 2–8 GHz using the coaxial method; the as-prepared powders were homogeneously mixed with molten paraffin wax to make a toroidal specimen with thickness of 3.00 mm and inner/outer diameter of 3.04/7.00 mm).

3. Results

3.1. Microstructure of M-MCNO

The synthesis procedure of the $\text{CoNiO}_2/\text{CoNi}$ co-decorating MXene hybrid is schematically shown in Figure 1. Thanks to a large number of reactive functional groups (e.g., -H, -F and -OH) on the MXene surfaces, Co^{2+} cations and Ni^{2+} cations can be easily and firmly anchored to the negatively charged MXene nanoflakes through electrostatic interac-

tions. Subsequently, HMT is slowly decomposed with increasing temperatures during the hydrothermal process. Heterogeneous nucleation and in situ growth of CoNi precursors could occur simultaneously under the controlled low supersaturation and weakly alkaline environment, thus guaranteeing an intertwining network of petal-like CoNi hydrate nanosheets anchored onto MXene nanoflakes. Upon annealing under an Ar atmosphere, the obtained CoNi hydrates can be converted into metal oxides and metal alloys. Meanwhile, the CoNiO₂ nanosheets form porous structures due to high-temperature dehydration decomposition. Eventually, the hierarchical heterogeneous structure of MXene nanoflakes loaded with CoNiO₂ nanosheets and CoNi nanoparticles is established.

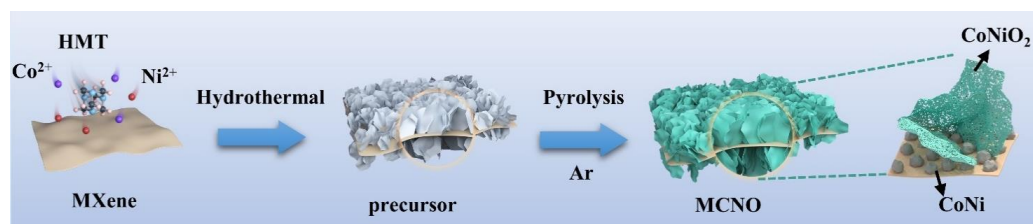


Figure 1. Schematic diagram of the MCNO composite's synthesis process.

The morphology characteristics of the MXene and M–MCNO hybrid were clarified by SEM. The single-layer morphology of the MXene nanoflake is shown in Figure 2a. Compared to the stacked flower-cluster architecture of L–MCNO (Figure S1a,b) and sparsely magnetic nanosheets/nanoparticles distributed in the H–MCNO (Figure S1c,d), M–MCNO hybrids inherit the layered morphology features of MXene nanoflakes and are covered with even, petal-like nanosheets on their surfaces (Figure 2b). A close-up observation (Figure 2b, the inset) clearly presents that those standing nanosheets are semi-transparent to the electron beam, indicating their ultrathin nature. These results verify that an appropriate dielectric dosage is crucial to ensure the formation of hierarchical heterostructures with dense, magnetic nanosheet arrays and well-dispersed ultrafine nanoparticles on the MXenes. Meanwhile, a close inspection reveals the presence of numerous micropores on the nanosheets, which are attributed to the evaporation of O and H elements from smooth precursor CoNi hydrates (Figure S2), leading the interleaved nanosheets to gradually shrink under thermal stress [21]. The formation of these pores exposes more active surfaces and increases more active sites, which can greatly enhance the polarization capacity of hybrids.

TEM observations (Figure 2c) further demonstrate the complex hierarchical architecture with abundant well-dispersed nanoparticles of ~90 nm (Figure 2c, inset) attaching to the surface of the MXene nanoflake, which is embedded in the dense network arrays of interlaced nanosheets. To further study the structural information of hybrids, an in-depth observation was conducted on the nanosheets at the edge region of the MXene (Figure 2d); a lattice fringe of 0.21 nm, highlighted with the yellow line, is detected in the petal-like nanosheets (Figure 2d, the inset), corresponding to the (200) planes of the CoNiO₂ phase [22]. Moreover, a lattice fringe of 0.20 nm, highlighted with a yellow line (Figure 2e) can be seen in the nanocrystals, corresponding to the (111) planes of CoNi nanocrystals (Figure 2e, inset) [23]. The distribution of petal-like CoNiO₂ nanoparticles and ultrafine CoNi nanocrystals on the MXene substrate was further elucidated by TEM images and corresponding EDS elemental images (Figure 2e,f). The multiply composition and architecture with CoNiO₂ nanosheets/CoNi nanoparticles co-decorating MXenes favor the enhancement of magnetic loss and heterogeneous interface polarization, boosting the attenuation of EM waves.

For further comparison, a control MXene/CNO sample prepared by mixing magnetic CNO with neat MXene nanoflakes is shown in Figure S3, which presents the morphology of multilayered stacked MXene flakes and agglomerated nanosheets, indicating that the structure-directing agent of MXene inhibits the agglomeration of CoNiO₂ nanosheets and CoNi nanoparticles and dominates the formation of the hierarchical architecture.

The interlaced CoNiO_2 nanosheets loaded on the MXene nanoflakes can guarantee the adequate formation of in-plane and out-of-plane void spaces. The uniformly ultrafine CoNi nanocrystals can increase the contact surface of the EM waves.

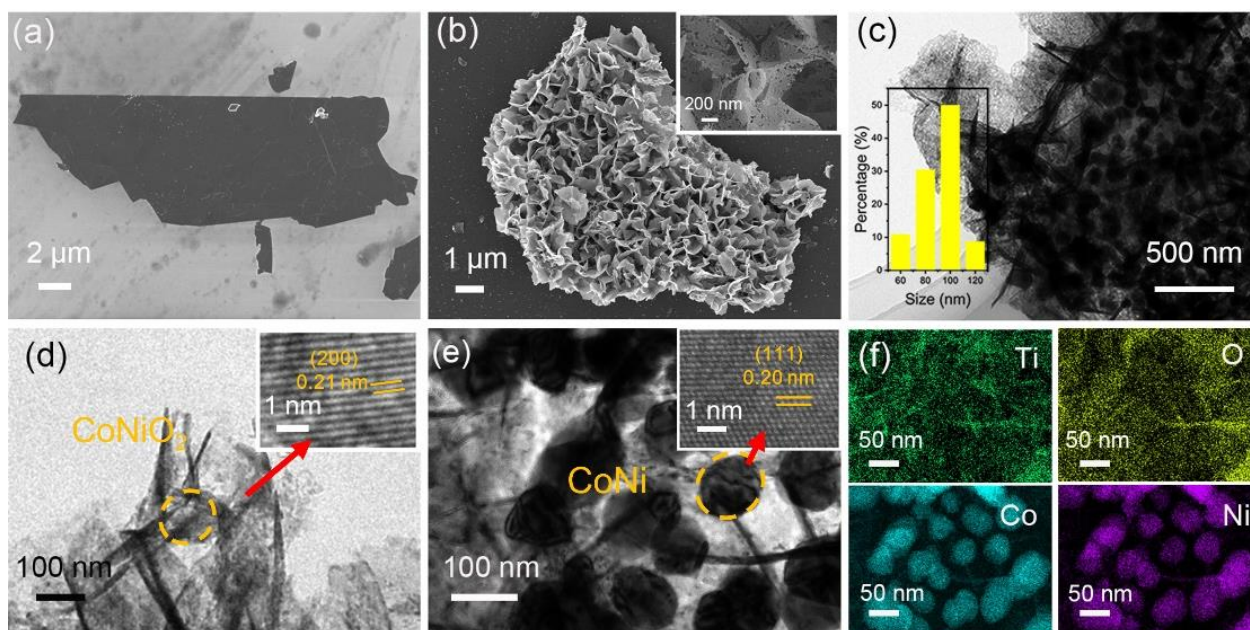


Figure 2. SEM images of: (a) a single-layered MXene nanoflake; (b) M-MCNO (the inset: a high magnification SEM image); (c–e) TEM images of M-MCNO (insets in (c): a size-distribution histogram of CoNi nanoparticles); (d): the lattice fringe of the CoNiO_2 nanosheets; (e): the lattice fringe of the CoNi nanoparticles); and (f) EDS elemental mapping images of M-MCNO.

To further confirm the composition and structure of the MCNO hybrids, the crystal phases of the obtained precursor and MCNO hybrids were authenticated by XRD. As shown in Figure 3a, the sharp peak at $\sim 6^\circ$ is ascribed to the MXene's (002) plane, and the strong peaks of the precursor at $2\theta = 12.7, 25.5, 32.9,$ and 58.9° can be assigned to (001), (002), (100), and (110) reflections of the CoNi -layer double hydroxides (CoNi-LDH) (JCPDS No. 74-1057 cobalt hydroxide and JCPDS No. 22-0752 nickel hydroxide), respectively [24,25]. All the characteristic peaks of the L-, M- and H-MCNO hybrids are remarkably similar, where peaks at $36.9, 42.9,$ and 62.2° can be accurately attributed to the CoNiO_2 phase (JCPDS: 10-0188), and peaks at 44.4 and 51.8° correspond to the Co phase (JCPDS No. 15-0806) and Ni phase (JCPDS No. 04-0850) without detectable impurities [22,26,27].

TG analysis was conducted under an Ar atmosphere to simulate the thermolysis of the precursor (Figure 3b); the curve reveals two distinct thermal decomposition processes occurring between $300\text{--}700^\circ\text{C}$. The first significant loss in mass (~ 9.68 wt %) occurs at around 300°C , followed by a negligible change in mass until 500°C . Then, further slow decomposition occurs between $500\text{--}700^\circ\text{C}$ (~ 3.03 wt %). Combined with the above XRD observation, these results support the conclusion that the two pyrolysis processes are the decomposition of CoNi hydrates and CoNiO_2 , respectively.

The elemental composition and surface chemical states of the M-MCNO sample were further confirmed by XPS. Note that the binding energy of the C 1s peak is usually calibrated using indeterminate carbon. However, this calibration method can lead to errors of up to 2.6 eV. Therefore, a high degree of caution should be applied to the conclusions when using the indeterminate carbon calibration method [28,29]. The full XPS spectrum proves the existence of Co and Ni elements in the M-MCNO (Figure 3c). In Figure 3d, the distinguishable peaks at 780.0, 795.83, 782.13 and 797.61 eV correspond to $\text{Co}^{2+} 2p_{3/2}$, $\text{Co}^{2+} 2p_{1/2}$, $\text{Co} 2p_{3/2}$, and $\text{Co} 2p_{1/2}$, respectively. Moreover, two satellites occur at 786.2 eV and 802.7 eV. These results verify the simultaneous presence of Co and CoO in the hybrid. Similarly,

six peaks of Ni 2p deconvoluted from the two CoNi and CoNiO₂ phases (Figure 3e) were fitted, which also indicates the coexistence of both Ni and NiO in the composite. The fitting peaks at 854.0 eV and 871.5 eV correspond to Ni 2p_{3/2} and 2p_{1/2}, respectively, whereas the peaks of 855.6 eV and 873.2 eV can be allocated to Ni-O 2p_{3/2} and 2p_{1/2}, respectively. Moreover, two satellites occur at 861.2 eV and 879.3 eV [30].

Typically, the higher the magnetization capacity, the stronger the magnetic attenuation property. Figure 3f shows the magnetic properties of L-, M-, H-MCNO, and M/CNO examined with a vibration sample magnetometer. All samples showcase the typical ferromagnetic hysteresis characteristics with saturation magnetization (M_s) of 49.1, 19.7, 9.3, and 20.7 emu/g, respectively. Obviously, the M_s values of these hybrids are positively correlated with the Co and Ni dosages. Meanwhile, it has been reported that the coercivity of magnetic material is mainly associated with magnetocrystalline features as well as defects [31]. Hence, due to the impressive magnetocrystalline anisotropy stemming from the well-dispersed magnetic nanosheets and nanoparticles onto MXene, M-MCNO has the highest H_c value.

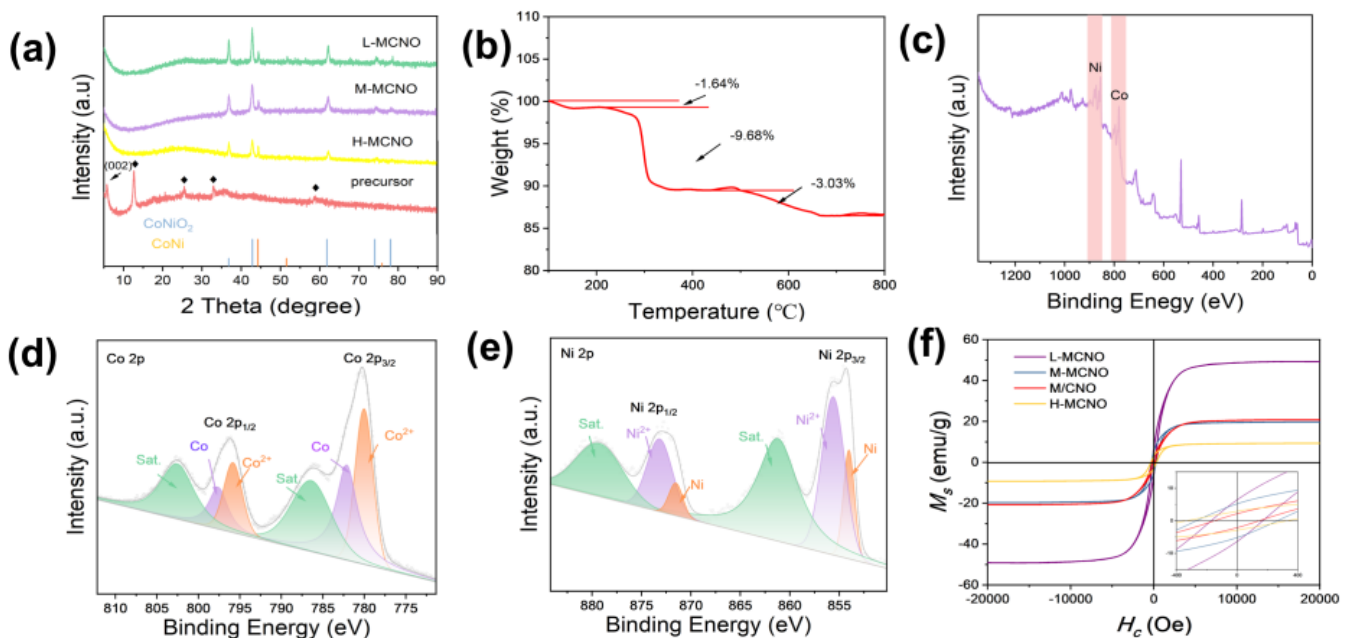


Figure 3. (a) XRD patterns; (b) TG curve in Ar atmosphere; and (c) XPS complete spectrum and high resolution (d) Co 2p and (e) Ni 2p XPS spectra of M-MCNO. (f) Magnetic hysteresis loop of L-, M-, H-MCNO and M/CNO.

3.2. Microwave Absorption Properties

Given the potential application of an absorber, it is essential to evaluate its RL value with the frequency. According to the transmission line theory, the RL value is calculated by the following equation involving the complex permittivity ($\epsilon_r = \epsilon' - j\epsilon''$) and the complex permeability ($\mu_r = \mu' - j\mu''$) [32–34]. Theoretically, 90% of incident waves can be absorbed when the RL value is less than -10 dB, and the corresponding frequency range is defined as the effective absorption bandwidth (EAB) [35], as follows:

$$RL = 20 \lg \left| \frac{Z_{in} - Z_0}{Z_{in} + Z_0} \right| \quad (1)$$

$$Z_{in} = Z_0 \sqrt{\frac{\mu_r}{\epsilon_r}} \tanh \left(j \frac{2\pi f d}{c} \sqrt{\mu_r \epsilon_r} \right) \quad (2)$$

where Z_{in} and Z_0 are the input impedances of the absorber and the characteristic impedance of the free space. f , d , and c are microwave frequency, thickness of the absorber, and the light velocity in free space, respectively.

The 3D RL curves of the neat MXene and composites are calculated and clarified (Figure 4a–e). As shown, the RL_{min} value of neat MXene is -3.68 dB at 9.06 GHz, while the RL can be neglected at a low frequency (Figure 4a), demonstrating a poor low-frequency EM absorption performance owing to the serious impedance mismatch and a single attenuation mechanism of conduction loss. For the MCNO hybrids, the RL values at a low frequency are significantly enhanced by modulating the ratio of MXene to magnets. In particular, the M–MCNO with a medium MXene loading exhibits the best low-frequency EM absorption capability, with an RL_{min} value of -45.33 dB (3.24 GHz) at a matched thickness of 5.0 mm (Figure 4c). As exhibited in Figure 4b,d, the composite absorber with lower MXene feeding corresponds to an RL value of -18.8 dB at 2.6 GHz, while the sample with a higher MXene content exhibits -38.6 dB at 6.2 GHz, demonstrating that decreasing or increasing the dielectric components in the absorber does not improve its low-frequency absorption capacity. In addition, the controlled sample of the M/CNO composite (Figure 4e) exhibits poor absorption performance, with an RL value of -6.6 dB at 4.5 GHz. According to the above analysis, the conclusion that can be arrived at is that designing a composite with a reasonable dielectric–magnetic dual-loss mechanism and a special hierarchical heterogeneous structure is essential to enhance the EM absorption performance at low frequencies.

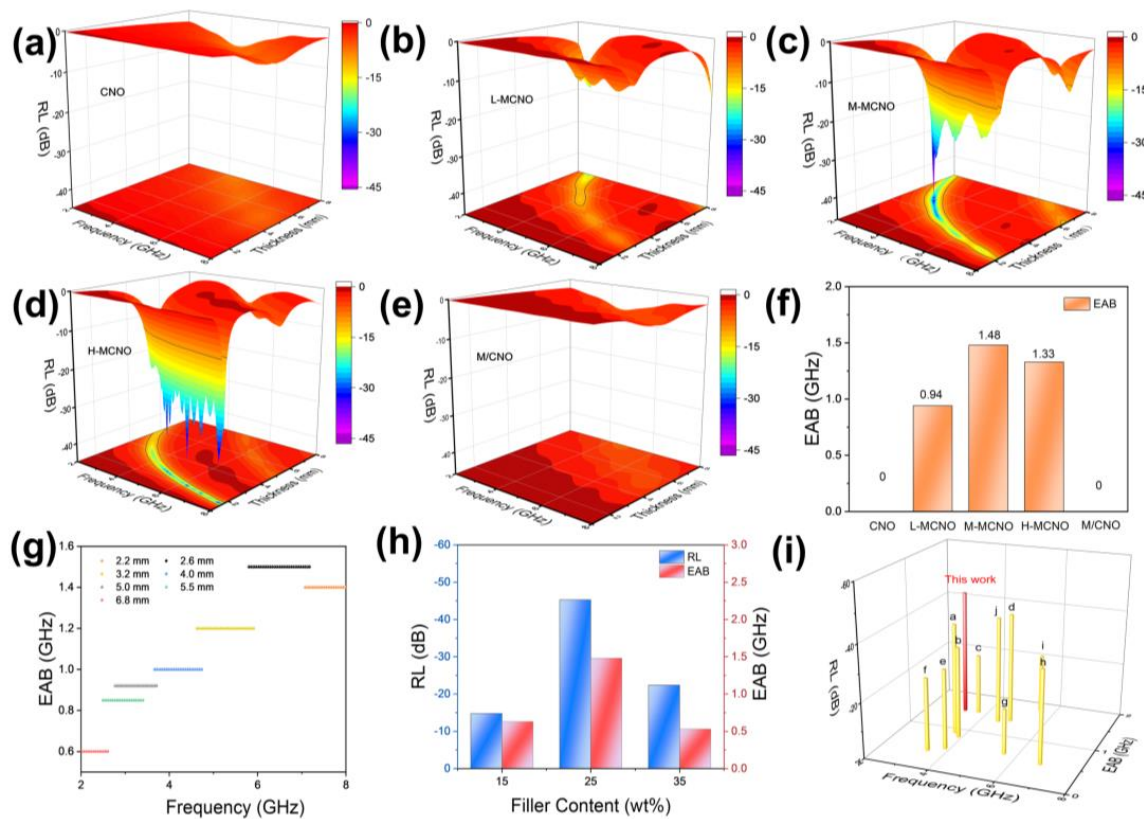


Figure 4. 3D RL curves of (a) neat MXene, (b) L–MCNO, (c) M–MCNO, (d) H–MCNO, and (e) M/CNO. (f) EAB of L–, M–, H–MCNO and M/CNO. (g) EAB of M–MCNO versus frequency at selected thicknesses. (h) Dependence of RL_{min} and EAB on filler contents for M–MCNO. (i) Comparison of EM absorption between M–MCNO and recently reported low-frequency absorbers.

Meanwhile, high-performance MAMs need to meet with the practical application to encompass wide microwave bands as much as possible. Figure 4f summarizes the maximum EAB (EAB_{max}) for all samples. Specifically, M–MCNO reached an EAB_{max} of 1.48 GHz, indicating that incorporating an appropriate quantity of dielectrics into the

hierarchical magnetized MXene is beneficial for expanding EAB. Figure 4g illustrates the variation in EAB of M-MCNO sample at selected matching thicknesses. It is worth noting that by tailoring the matching thicknesses from 2.0 to 7.0 mm, the EAB of M-MCNO sample can be extended to entirely cover the S-band and C-band. The impressive low-frequency microwave absorption performance of the M-MCNO absorber is strongly demonstrated by these analytical results. Considering that the filler amount of absorber also affects the EM absorption performance, we further explore the RL value and EAB of M-MCNO composites with filler contents of 15, 25, and 35 wt %. As shown in Figure 4h, with the filler content increasing, the RL and EAB values increase and then decrease. Clearly, the microwave absorption properties of the 25 wt % sample performs better than the other samples. It should be noted that the M-MCNO hybrid exhibits better low-frequency absorption ability, wider EAB and thinner thickness than most of the latest research reported low-frequency materials (Figure 4i and Table S1), indicating its potential for brilliant low-frequency MAMs.

The EM parameters involve relative complex permittivity ($\epsilon_r = \epsilon' - j\epsilon''$) and relative complex permeability ($\mu_r = \mu' - j\mu''$), which can be used to evaluate the MAMs' EM characteristics. Generally, the real part of the complex permittivity or permeability (ϵ' or μ') stands for the storage capability of EM energy, while the imaginary part (ϵ'' or μ'') represents the dissipation capability of EM energy [36]. Among all the samples, the neat MXene sample exhibits the highest values of ϵ' and ϵ'' across the entire frequency range (Figure S4a), indicating its significant dielectric loss. However, the magnetic loss of the neat MXene sample can be considered negligible (Figure S4b). The great imbalance in the EM parameters gives rise to the serious impedance mismatch, resulting in the microwaves' reflection on the MAMs rather than their penetration into the interior for attenuation. Unsurprisingly, after anchoring the magnetic CoNiO₂ nanosheet arrays and CoNi nanoparticles onto their surfaces, the ϵ' and ϵ'' values (Figure 5a,b) of the magnetized hybrids fall slightly while the μ' and μ'' values (Figure 5d,e) are enhanced compared to the neat MXene nanoflakes. This change aids in harmonizing permittivity and permeability to perfect impedance-matching. Additionally, both the ϵ' and ϵ'' values are positively correlated with the MXene contents in the samples. With the increase in frequency, both ϵ' and ϵ'' values decrease, exhibiting similar dispersion behavior. The trend can be explained by the fact that the polarization response cannot vary with the electric field change [37,38]. However, note that the ϵ'' of H-MCNO fluctuates significantly with increasing the frequency, which is caused by the polarization loss resulting from the exposure of the barer MXene. In addition, under the conditions that the Co and Ni content in the M-MCNO sample is similar to M/CNO (Figure S5), the unique interleaved heterostructure of M-MCNO results in higher ϵ' and ϵ'' values than M/CNO (Figure 5a,b). The dielectric loss capacity is influenced by the conduction and polarization losses and is typically represented by the dielectric loss tangent value ($\tan\delta_e$) [39]. As illustrated in Figure 5c, the $\tan\delta_e$ values of L-, M-, and H-MCNO exhibit similar trends to the variation of ϵ'' , maintaining four peaks at 3.2, 4.8, 6.7, and 7.7 GHz. Based on the aforementioned investigations, all MCNO samples exhibit superior dielectric loss, which is mainly attributed to two factors: (1) The 3D interconnected conductive network facilitates free electron migration, enhancing the conduction loss. That is to say, the migrating electrons can move on the surfaces of the MXene nanoflakes, CoNiO₂ nanosheets, and CoNi nanoparticles, whereas the leaped electrons can bypass defects in MXene or jump to CoNiO₂ nanosheets and CoNi nanoparticles, resulting in the formation of a dense microcurrent network [37,40–42]; and (2) The introduction of dual-phase CoNiO₂ and CoNi nanocrystals in the vicinity of MXene nanoflakes forms abundant heterojunction interfaces, enhancing interface polarization and hindering the self-aggregation of adjacent MXene flakes, exposing more surface defects and functional groups, amplifying dipole polarization [43–45]. (3) The highly exfoliated MXene and the abundant pores of the CoNiO₂ nanosheets can provide massive defects, enlarging its polarization loss.

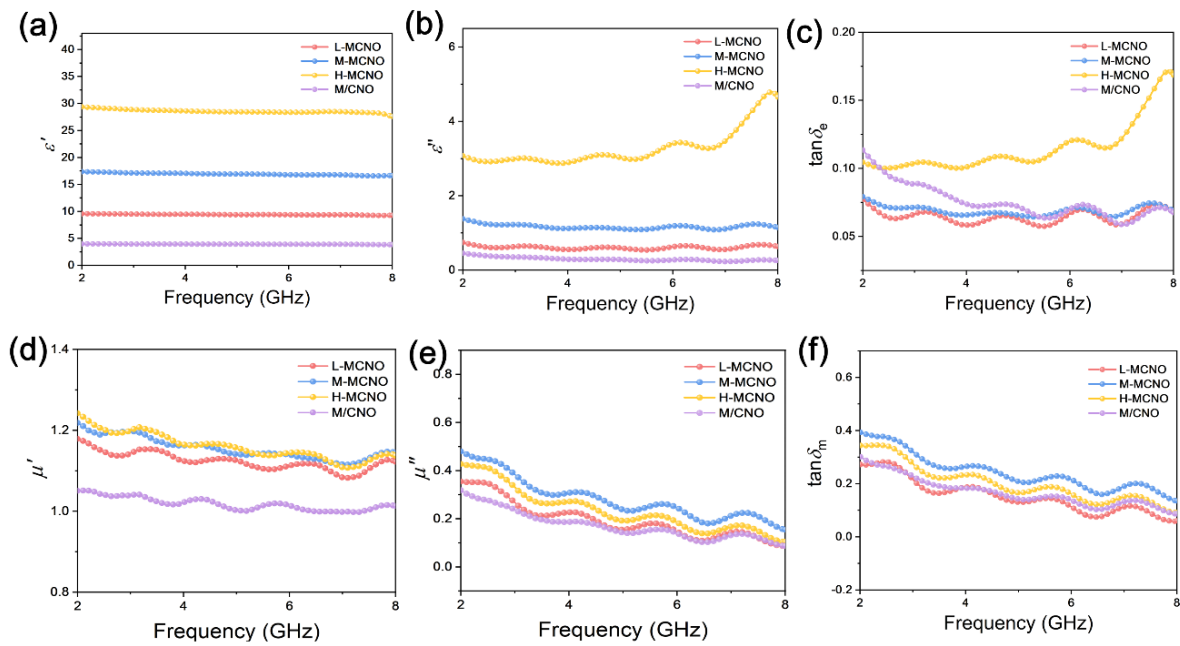


Figure 5. (a) ϵ' , (b) ϵ'' , (c) $\tan\delta_e$, (d) μ' , (e) μ'' , and (f) $\tan\delta_m$ values as a function of the frequency for L-, M-, H-MCNO and M/CNO.

The Debye relaxation model is introduced to further analyze the dielectric loss mechanism of the absorber and is described as follows [46]:

$$\epsilon' = \epsilon_{\infty} + \frac{\epsilon_s - \epsilon_{\infty}}{1 + (2\pi f)^2 \tau^2} \quad (3)$$

$$\epsilon'' = \frac{2\pi f \tau (\epsilon_s - \epsilon_{\infty})}{1 + (2\pi f)^2 \tau^2} \quad (4)$$

$$\left(\epsilon' - \frac{\epsilon_s + \epsilon_{\infty}}{2}\right)^2 + (\epsilon'')^2 = \left(\frac{\epsilon_s - \epsilon_{\infty}}{2}\right)^2 \quad (5)$$

where ϵ_s represents static permittivity and ϵ_{∞} represents the relative permittivity. Among the as-prepared samples, the $\epsilon' - \epsilon''$ curve is almost made up of sloping lines and deformed semicircles (Figure S6). The appearance of the former can be ascribed to the conductive losses, whereas the latter can mainly correspond to a Debye relaxation process related to polarization losses [47]. It is obvious that the Cole–Cole semicircle number of MCNO hybrids is significantly more than that of neat MXene nanoflakes. The L-, M- and H-MCNO samples exhibit Cole–Cole semicircles and sloping lines, signifying polarization and conduction loss exist simultaneously.

The μ' and μ'' values of the magnetized MXene in the frequency range 2–8 GHz can intervene 1.0–1.3 and 0–0.5 (Figure 5d,e), manifesting its excellent magnetic loss capacity at the S-band and C-band. It is noteworthy that the $\tan\delta_m$ and μ'' values (Figure 5e,f) for all samples maintain a similar trend and fluctuate between 0.0 and 0.6. When comparing $\tan\delta_e$ with $\tan\delta_m$, the magnetic loss accounts for the major contribution in the low frequency for all magnetized samples. In general, eddy current loss, natural resonance, and exchange resonance are the main magnetic loss mechanisms in the 2–8 GHz range [48]. If only eddy current loss is present, the C_0 value will remain constant and independent of the frequency [13]. In Figure S7, it can be observed that the C_0 value of the sample decreases significantly with increasing frequencies in the 2–8 GHz range, indicating the presence of eddy current loss as well as natural resonance and exchange resonance.

Perfect impedance-matching and strong attenuation ability are two major principles for designing high-performance MAMs [3]. Impedance-matching represents the capacity

of the EM waves to enter the absorber, and attenuation capacity indicates the degree of EM wave attenuation loss [49]. Based on the transmission line theory, we calculate the normalized impedance-matching ($Z = Z_{in}/Z_0$) and attenuation constant (α) for all the samples by the following equations [50]:

$$\alpha = \frac{\sqrt{2}\pi f}{c} \sqrt{\left(\epsilon''\mu'' - \epsilon'\mu' + \sqrt{(\epsilon''\mu'' - \epsilon'\mu')^2 + (\epsilon'\mu'' + \epsilon''\mu')^2}\right)} \quad (6)$$

The Z and α curves for magnetized MXene samples are illustrated at their optimal match thickness in Figure 6a,b. Typically, when the Z value is close to 1, almost all incident EM waves can penetrate into the material [51]. The neat MXene samples, with large ϵ' and ϵ'' , have the best attenuation ability, while the impedance-matching is poor in the other studied samples (Figure S8), exhibiting the worst EM absorption properties. For comparison, the L-, M- and H-MCNO samples exhibit more optimal impedance-matching and moderate attenuation ability after the introduction of magnetic components. Specially, M-MCNO illustrates the best impedance-matching ($Z \approx 1$) and impressive attenuation capacity within low frequencies, leading to outstanding absorption performance. The above results show that introducing magnetic components is essential to perfecting optimal impedance-matching. In addition, M/CNO, with a similar Co-Ni content but with aggregation of MXene nanoflakes and magnetic crystallites, shows worse impedance-matching and has a poor attenuation capacity, demonstrating that constructing a rational structure is crucial to obtain impressive EM absorption properties at low frequencies. Specifically, the hierarchical structure guarantees sufficient exposure of the polar functional groups on the MXene surface, and appropriate loading of the magnetic phases and the multiple reflections of EM waves, performing the best impedance-matching owing to the reasonable ϵ and μ values when compared to other samples.

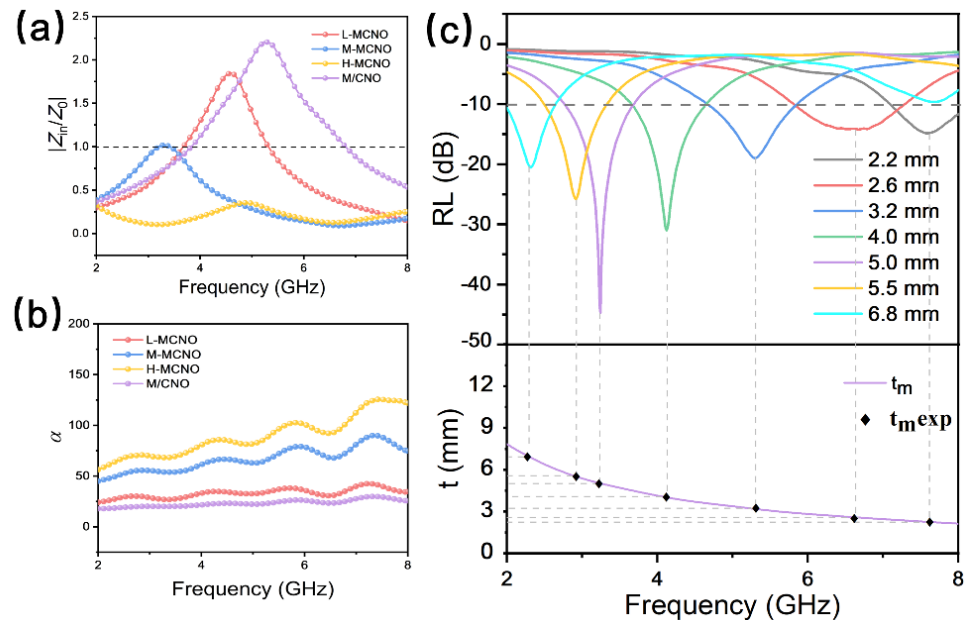


Figure 6. (a) $|Z_{in}/Z_0|$ and (b) α as a function of frequency for L-, M-, H-MCNO and M/CNO. (c) Dependence of matching thickness (t_m) on frequency (f_m) for M-MCNO under $\lambda/4$.

In addition, we describe the relationship between the RL intensity (dB) and the thickness (t_m) with frequency (f_m), which can be expressed by the following [52]:

$$t_m = \frac{n\lambda}{4} = \frac{nc}{\left(4f_m \sqrt{|\mu_r||\epsilon_r|}\right)} \quad (n = 1, 3, 5, \dots) \quad (7)$$

where λ denotes the wavelength of the EM wave. When t_m and f_m satisfy Equation (7), the reflection of EM waves on the air interface will have an interference effect with the incident EM waves, leading to mutual cancellation of the EM waves inside the absorber [23]. As predicted, the peak of the RL_{\min} shifts towards a lower frequency, increasing with the matching thickness (Figure 6c). The experimental thickness (t_m^{exp} , labeled with a diamond) is identical to the simulated thickness, demonstrating that the EM wave dissipation of M-MCNO is consistent with the quarter-wavelength cancellation theory and produces brilliant reflection losses.

In practical applications, the radar waves emitted by the radar detector are partially absorbed and partially reflected by the invisible coating on the target's surface (Figure 7a). The RCS area of the target can be equated to the projected area of the metal sphere with the same echo signal and can be expressed in terms of one square meter of the reflection loss value. Figure 7b–e shows the CST simulation results of L-, M- and H-MCNO attached to a perfect electric conductor (PEC) layer, referring to their microwave dissipation ability in the real far field. Among them, PEC demonstrates the largest RCS value. After being covered with MCNO, the RCS values of the as-fabricated samples are significantly reduced, proving that L-, M- and H-MCNO can effectively decrease the radar scattering intensity. As expected, the M-MCNO sample exhibits the lowest RCS value in the angular range and achieves lower -10 dB in the ranges of $-90^\circ < \theta < -7^\circ$ and $7^\circ < \theta < 90^\circ$ (Figure 7f). Furthermore, when $\theta = 0^\circ$, the maximum RCS reduction in the M-MCNO is 7.4 dB m^2 . Therefore, the synthesized M-MCNO, with an appropriate composition and architecture, allows for the reflection from incident EM waves from PEC surfaces to be suppressed, exhibiting excellent radar wave attenuation.

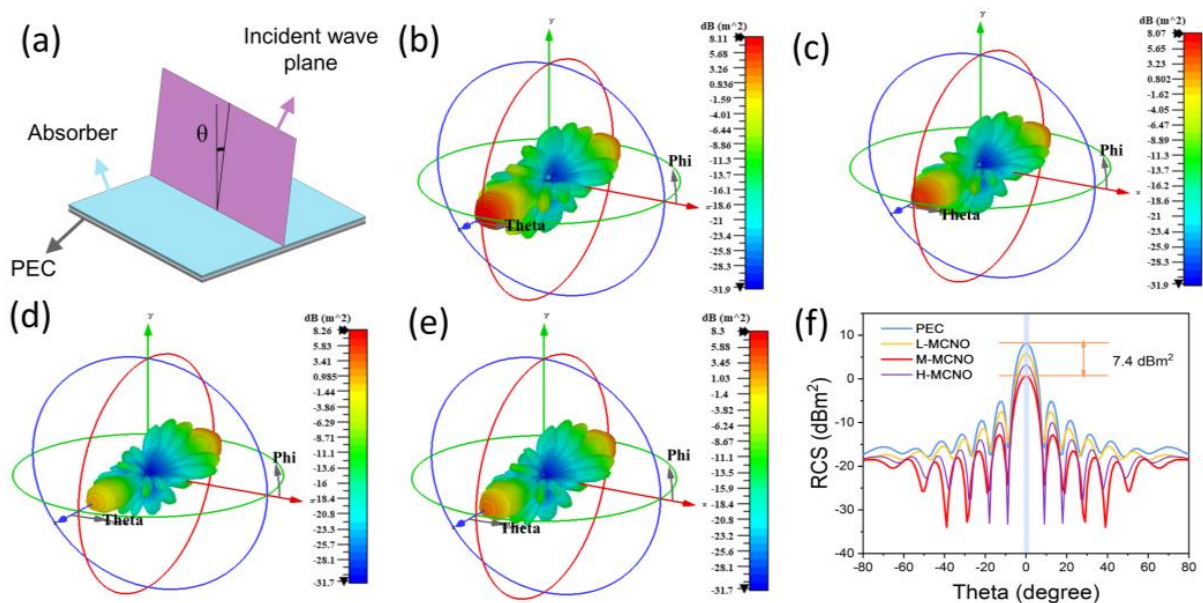


Figure 7. (a) Working principle of radar detectors. CST simulation results of: (b) PEC; (c) L-MCNO/PEC; (d) M-MCNO/PEC; (e) H-MCNO/PEC; and (f) simulated RCS curves of the PEC, L-, M- and H-MCNO under the conditions of $-90^\circ < \theta < +90^\circ$. The arrows are for the highest and lowest values that the CST calculates.

The EM absorption mechanism of multicomponent monolayer MXene nanoflakes loaded with magnetic nanosheets and nanoparticles is illustrated in Figure 8. First, the anisotropy energy induced by the petal-like CoNiO_2 magnetic nanosheets and uniformly ultrafine CoNi magnetic nanocrystals can magnify low-frequency magnetic loss capacity through eddy current loss, natural resonance, and exchange resonance [53,54]. Second, the multi-component magnetic arrays with poor conduct can also constrain the excessive permittivity of MXene. The valid complementarity of the EM parameters refines the

low-frequency impedance-matching [55]. Third, the complex hierarchical heterostructure hinders the agglomeration of MXene and magnetic components and guarantees sufficient in-plane and out-of-plane voids. When penetrating such a structure, the entering EM waves are confined within the absorber, leading to multiple reflections and scatterings, effectively increasing the dissipation of EM wave energy [56–58]. Fourth, the hierarchical structure assembled from three components with different EM parameters offers a large number of heterojunctions, resulting in the accumulation of free electrons to promote interfacial polarization [59]. Fifth, well-dispersed magnetic nanosheets and nanograins grow on the surface of MXene to form an interleaved conductive network, which allows the excited electrons induced by the alternating electromagnetic field to migrate or jump rapidly, improving the conduction loss [60]. In addition, the intrinsic high conductance of the monolayer MXene can endow the as-prepared M–MCNO with superior conduction loss. Finally, the highly exfoliated MXene nanoflakes and abundant pores of the CoNiO₂ nanosheets can result in significant defects, amplifying its polarization loss [21]. Therefore, the synergistic effect of impressive impedance-matching and attenuation capabilities significantly enhances the absorption ability of M–MCNO in the S-band and C-band.

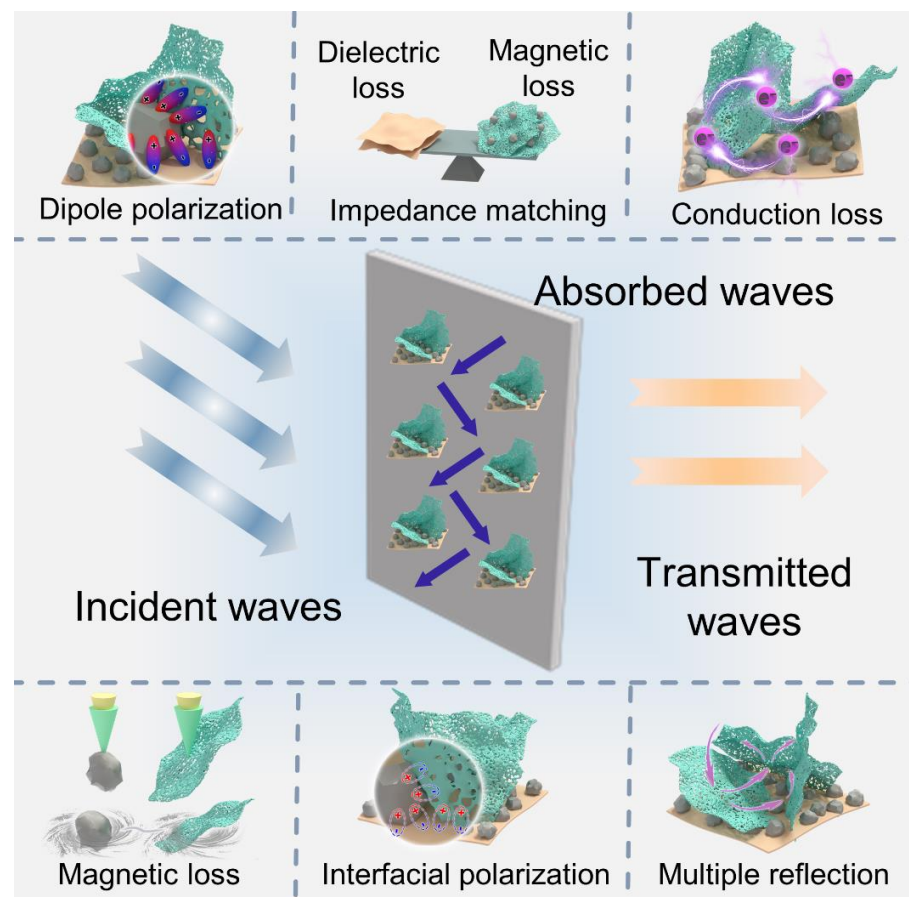


Figure 8. Schematic of microwave absorption mechanisms of M–MCNO.

4. Conclusions

In this work, we prepared hierarchical, heterostructured monolayer MXene loaded with magnetic nanosheets (CoNiO₂) and nanoparticles (CoNi) by hydrothermal and pyrolytic processes. CoNiO₂ nanosheet arrays were randomly staggered on both sides of the monolayer MXene, while CoNi nanocrystals were uniformly distributed onto the MXene nanoflakes. Benefiting from the superior magnetocrystalline anisotropy of well-dispersed magnetic nanosheets and nanocrystals, as well as the perfect hierarchical heterostructure, the as-synthesized absorber exhibits impressive magnetic loss, conduction loss, interfacial

polarization, and dipolar polarization, and balanced impedance-matching. This superior M–MCNO has an excellent EM absorption capability with an RL value of -45.33 dB (3.24 GHz) and a matching thickness of 5.0 mm. Moreover, the EAB of the M–MCNO sample can entirely cover the S-band and C-band by tailoring the matching thicknesses from 2 to 7 mm. In addition, the M–MCNO can reduce satellite RCS values over multiple angles to meet stealth requirements in the low-frequency range and reduce the risk of detection of satellites in orbit. This work provides a unique approach for preparing advanced MXene-based low-frequency microwave absorbing materials for portable communication devices in the civil field.

Supplementary Materials: The following supporting information can be downloaded at: <https://www.mdpi.com/article/10.3390/coatings14050631/s1>, Figure S1. SEM images of (a,b) L–MCNO and (c,d) H–MCNO; Figure S2. SEM image of CoNi hydrate. Figure S3. SEM image of M/CNO. Figure S4. (a) ϵ' and ϵ'' , and (b) μ' and μ'' curves of neat MXene. Figure S5. XPS surveys of M–MCNO and M/CNO. Figure S6. $\epsilon'-\epsilon''$ plots of (a) neat MXene, (b) L–MCNO, (c) M–MCNO, and (d) H–MCNO. Figure S7. C_0 of L–, M–, H–MCNO and M/CNO. Figure S8. (a) Z_{in}/Z_0 and (b) α of MXene. Table S1. Comparison of microwave absorption properties of M–MCNO hybrid with recently reported dielectric-magnetic composites. (References [61–66] are cited in Supplementary Materials).

Author Contributions: Conceptualization, D.L.; methodology, L.D.; validation, Y.S., W.Z. and H.L.; investigation, L.D.; resources, R.X.; data curation, L.D.; writing—original draft preparation, L.D.; writing—review and editing, R.X.; supervision, R.X. and D.L.; project administration, R.X.; funding acquisition, W.J. All authors have read and agreed to the published version of the manuscript.

Funding: This research was funded by the National Natural Science Foundation of China (No. 62171331).

Institutional Review Board Statement: Not applicable.

Informed Consent Statement: Not applicable.

Data Availability Statement: The raw data supporting the conclusions of this article will be made available by the authors on request.

Conflicts of Interest: The authors declare no conflict of interest.

References

1. Zhang, S.J.; Li, J.Y.; Jin, X.T.; Wu, G.L. Current advances of transition metal dichalcogenides in electromagnetic wave absorption: A brief review. *Int. J. Min. Met. Mater.* **2023**, *30*, 428–445. [CrossRef]
2. Liu, W.; Tan, S.J.; Yang, Z.H.; Ji, G.B. Enhanced low-frequency electromagnetic properties of MOF-derived cobalt through interface design. *ACS Appl. Mater. Interfaces* **2018**, *10*, 31610–31622. [CrossRef] [PubMed]
3. Li, J.; Wu, Q.; Wang, X.Y.; Wang, B.L.; Liu, T. Metal-organic framework-derived Co/CoO nanoparticles with tunable particle size for strong low-frequency microwave absorption in the S and C bands. *J. Colloid Interface Sci.* **2022**, *628*, 10–21. [CrossRef] [PubMed]
4. Yang, B.T.; Fang, J.F.; Xu, C.Y.; Cao, H.; Zhang, R.X.; Zhao, B.; Huang, M.Q.; Wang, X.Y.; Lv, H.L.; Che, R.C. One-dimensional magnetic FeCoNi alloy toward low-frequency electromagnetic wave absorption. *Nano-Micro Lett.* **2022**, *14*, 170. [CrossRef]
5. Dong, Y.Q.; Liang, X.C.; Zhong, S.J.; Yu, M.J.; Wang, C.G. A simple method for preparing flaky FeSiAl for low-frequency electromagnetic wave absorber. *J. Magn. Magn. Mater.* **2023**, *574*, 170676. [CrossRef]
6. Sun, X.H.; Zhao, X.Y.; Zhang, X.Y.; Wu, G.H.; Rong, X.H.; Wang, X.W. TiO₂ nanosheets/Ti₃C₂T_x MXene 2D/2D composites for excellent microwave absorption. *ACS Appl. Nano Mater.* **2023**, *6*, 14421–14430. [CrossRef]
7. Dai, Y.; Wu, X.; Liu, Z.; Zhang, H.B.; Yu, Z.Z. Highly sensitive, robust and anisotropic MXene aerogels for efficient broadband microwave absorption. *Compos. Part B-Eng.* **2020**, *200*, 108263. [CrossRef]
8. Yu, G.Y.; Shao, G.F.; Chen, Y.; Huang, X.G. Nanolayered ceramic-confined graphene aerogel with conformal heterointerfaces for low-frequency microwave absorption. *ACS Appl. Mater. Interfaces* **2023**, *15*, 39559–39569. [CrossRef]
9. Hou, M.M.; Du, Z.J.; Liu, Y.; Ding, Z.Z.; Huang, X.Z.; Chen, A.L.; Zhang, Q.C.; Ma, Y.T.; Lu, S.J. Reduced graphene oxide loaded with magnetic nanoparticles for tunable low frequency microwave absorption. *J. Alloys Compd.* **2022**, *913*, 165137. [CrossRef]
10. Lei, B.Y.; Hou, Y.L.; Meng, W.J.; Wang, Y.Q.; Yang, X.X.; Ren, M.X.; Zhao, D.L. Hierarchical bath lily-like hollow microspheres constructed by graphene and Fe₃O₄ nanoparticles with enhanced broadband and highly efficient low-frequency microwave absorption. *Carbon* **2022**, *196*, 280–289. [CrossRef]
11. Wang, L.; Chen, Z.; Wang, X.; Zhang, L.Y.; Zhang, Z.T.; Zhao, Q.; Gao, Y.F. Fe₃O₄@C 3D foam for strong low-frequency microwave absorption. *J. Mater.* **2023**, *9*, 148–156. [CrossRef]

12. Xiang, Z.C.; Song, Z.; Wang, T.S.; Feng, M.H.; Zhao, Y.J.; Zhang, Q.T.; Hou, Y.; Wang, L.X. Bead-like flexible ZIF-67-derived Co@Carbon composite nanofibre mat for wideband microwave absorption in C-band. *Carbon* **2024**, *216*, 118573. [[CrossRef](#)]
13. Wang, Y.; Zhang, H.Y.; Wu, Q.B.; Li, S.K.; Gao, H.; Wan, B.S.; Wen, D.F.; Zeng, G.X. Magnetic enhanced high-efficiency electromagnetic wave absorbing MXene/Fe₃O₄ composite absorbers at 2–40 GHz. *J. Mater. Chem. C* **2023**, *11*, 4171–4181. [[CrossRef](#)]
14. Wang, X.Y.; Xing, X.F.; Zhu, H.S.; Li, J.; Liu, T. State of the art and prospects of Fe₃O₄/carbon microwave absorbing composites from the dimension and structure perspective. *Adv. Colloid Interface Sci.* **2023**, *318*, 102960. [[CrossRef](#)] [[PubMed](#)]
15. Xia, Y.X.; Gao, W.W.; Gao, C. A review on graphene-based electromagnetic functional materials: Electromagnetic wave shielding and absorption. *Adv. Funct. Mater.* **2022**, *32*, 2204591. [[CrossRef](#)]
16. Liu, J.M.; Yu, W.Z.; Zhao, Z.H.; Liu, D.; Liu, S.S.; Wang, J.; Ma, M.L.; Yu, Q.H.; Yang, N.T. 3D honeycomb Fe/MXene derived from prussian blue microcubes with a tunable structure for efficient low-frequency and flexible electromagnetic absorbers. *ACS Appl. Mater. Interfaces* **2023**, *15*, 48519–48528. [[CrossRef](#)]
17. Pan, F.; Rao, Y.P.; Batalu, D.; Cai, L.; Dong, Y.Y.; Zhu, X.J.; Shi, Y.Y.; Shi, Z.; Liu, Y.W.; Lu, W. Macroscopic electromagnetic cooperative network-enhanced MXene/Ni chains aerogel-based microwave absorber with ultra-low matching thickness. *Nano-Micro Lett.* **2022**, *14*, 140. [[CrossRef](#)] [[PubMed](#)]
18. Yi, Q.J.; Zhang, F.; Song, Y.N.; Wang, X.; Zhang, H.; Li, C.L.; Piao, M.X. One-step synthesis of cobalt nanosheets depositing with carbon microsphere by microwave plasma assisted reduction chemical vapor deposition technique against electromagnetic pollution. *Carbon* **2023**, *214*, 118322. [[CrossRef](#)]
19. Liu, P.B.; Gao, S.; Zhang, G.Z.; Huang, Y.; You, W.B.; Che, R.C. Hollow engineering to Co@N-doped carbon nanocages via synergistic protecting-etching strategy for ultrahigh microwave absorption. *Adv. Funct. Mater.* **2021**, *31*, 202102812. [[CrossRef](#)]
20. Qu, Y.G.; Liu, Z.Y.; Li, X.; Si, Y.; Xu, R.X.; Liu, D. Ultrafine well-dispersed Co nanocrystals onto crumpled sphere-like rGO for superior low-frequency microwave absorption. *Carbon* **2023**, *213*, 118280. [[CrossRef](#)]
21. Wang, S.P.; Liu, Z.Y.; Liu, Q.C.; Wang, B.J.; Wei, W.; Wu, H.; Xu, Z.J.; Li, S.K.; Huang, F.Z.; Zhang, H. Promoting the microwave absorption performance of hierarchical CF@NiO/Ni composites via phase and morphology evolution. *Int. J. Min. Met. Mater.* **2023**, *30*, 494–503. [[CrossRef](#)]
22. Zhang, N.; Qi, S.Y.; Guo, Y.F.; Wang, P.F.; Ren, N.; Yi, T.F. Approaching high-performance lithium storage materials of CoNiO₂ microspheres wrapped coal tar pitch-derived porous carbon. *Dalton Trans.* **2023**, *52*, 8704–8715. [[CrossRef](#)]
23. Liu, Z.K.; Chen, J.; Que, M.D.; Zheng, H.Q.; Yang, L.F.; Yuan, H.D.; Ma, Y.Z.; Li, Y.J.; Yang, X.F. 2D Ti₃C₂T_x MXene/MOFs composites derived CoNi bimetallic nanoparticles for enhanced microwave absorption. *Chem. Eng. J.* **2022**, *450*, 138442. [[CrossRef](#)]
24. Ye, S.Z.; Guan, X.F. HMT-controlled synthesis of mesoporous NiO hierarchical nanostructures and their catalytic role towards the thermal decomposition of ammonium perchlorate. *Appl. Sci.* **2019**, *9*, 2599. [[CrossRef](#)]
25. Cho, E.C.; Chang-Jian, C.-W.; Huang, J.H.; Chou, J.A.; Syu, W.L.; Chen, Y.L.; Lee, K.C.; Hsiao, Y.S. Phase and morphology control in the synthesis of Co₃O₄ nanosphere/ α -Co(OH)₂ nanosheet hybrids for application in supercapacitors. *J. Taiwan Inst. Chem. Eng.* **2020**, *110*, 163–172. [[CrossRef](#)]
26. Chang, M.; Jia, Z.R.; Wu, G.L.; Yin, P.F. Multiple dimension-component designed Co/Co₉S₈/Ti₃C₂T_x MXene composite for enhanced microwave absorption. *Appl. Phys. Lett.* **2023**, *122*, 131901. [[CrossRef](#)]
27. Liang, L.Y.; Han, G.J.; Li, Y.; Zhao, B.; Zhou, B.; Feng, Y.Z.; Ma, J.M.; Wang, Y.M.; Zhang, R.; Liu, C.T. Promising Ti₃C₂T_x MXene/Ni chain hybrid with excellent electromagnetic wave absorption and shielding capacity. *ACS Appl. Mater. Interfaces* **2019**, *11*, 25399–25409. [[CrossRef](#)] [[PubMed](#)]
28. Evans, S. Estimation of the uncertainties associated with XPS peak intensity determination. *Surf. Interface Anal.* **2004**, *18*, 323–332. [[CrossRef](#)]
29. Greczynski, G.; Hultman, L. Compromising Science by Ignorant Instrument Calibration—Need to Revisit Half a Century of Published XPS Data. *Angew. Chem. Int. Ed.* **2020**, *59*, 5002–5006. [[CrossRef](#)]
30. Zeng, X.J.; Zhao, C.; Yin, Y.C.; Nie, T.L.; Xie, N.H.; Yu, R.H.; Stucky, G.D. Construction of NiCo₂O₄ nanosheets-covered Ti₃C₂T_x MXene heterostructure for remarkable electromagnetic microwave absorption. *Carbon* **2022**, *193*, 26–34. [[CrossRef](#)]
31. Liu, Z.Q.; Xiao, K.; Xu, Q.Z.; Li, N.; Su, Y.Z.; Wang, H.J.; Chen, S. Fabrication of hierarchical flower-like super-structures consisting of porous NiCo₂O₄ nanosheets and their electrochemical and magnetic properties. *RSC Adv.* **2013**, *3*, 4372–4380. [[CrossRef](#)]
32. Wu, F.; Wan, L.Y.; Wang, T.; Tariq, M.R.; Shah, T.; Liu, P.; Zhang, Q.Y.; Zhang, B.L. Construction of binary assembled MOF-derived nanocages with dual-band microwave absorbing properties. *J. Mater. Sci. Technol.* **2022**, *117*, 36–48. [[CrossRef](#)]
33. Fan, B.X.; Xing, L.; He, Q.M.; Zhou, F.J.; Yang, X.F.; Wu, T.; Tong, G.X.; Wang, D.M.; Wu, W.H. Selective synthesis and defects steering superior microwave absorption capabilities of hollow graphitic carbon nitride micro-polyhedrons. *Chem. Eng. J.* **2022**, *435*, 135086. [[CrossRef](#)]
34. Fan, B.B.; Ansar, M.T.; Chen, Q.Q.; Wei, F.C.; Du, H.; Ou, Y.B.; Kan, E.J.; Chen, Y.Q.; Zhao, B.; Zhang, R. Microwave-assisted hydrothermal synthesis of 2D/2D MoS₂/Ti₃C₂T_x heterostructure for enhanced microwave absorbing performance. *J. Alloys Compd.* **2022**, *923*, 166253. [[CrossRef](#)]
35. He, F.L.; Zhao, W.; Cao, L.; Liu, Z.F.; Sun, L.Q.; Zhang, Z.Y.; Zhang, H.; Qi, T. The ordered mesoporous barium ferrite compounded with nitrogen-doped reduced graphene oxide for microwave absorption materials. *Small* **2023**, *19*, 2205644. [[CrossRef](#)]

36. Guo, H.T.; Wang, X.; Pan, F.; Shi, Y.Y.; Jiang, H.J.; Cai, L.X.; Cheng, J.; Zhang, X.; Yang, Y.; Li, L.; et al. State of the art recent advances and perspectives in 2D MXene-based microwave absorbing materials: A review. *Nano Res.* **2023**, *16*, 10287–10325. [[CrossRef](#)]
37. Cheng, J.B.; Liu, B.W.; Wang, Y.Q.; Zhao, H.B.; Wang, Y.Z. Growing CoNi nanoalloy@N-doped carbon nanotubes on MXene sheets for excellent microwave absorption. *J. Mater. Sci. Technol.* **2022**, *130*, 157–165. [[CrossRef](#)]
38. Zhang, L.; Stalin, N.; Tran, N.; Mehrez, S.; Badran, M.F.; Mohanavel, V.; Xu, Q. Development of high-efficient double-layer microwave absorbers based on 3D cabbage-like CoFe₂O₄ and cauliflower-like polypyrrole. *Ceram. Int.* **2022**, *48*, 16374–16385. [[CrossRef](#)]
39. Zou, Z.; Ning, M.Q.; Lei, Z.K.; Zhuang, X.H.; Tan, G.; Hou, J.J.; Xu, H.; Man, Q.K.; Li, J.B.; Li, R.W. 0D/1D/2D architectural Co@C/MXene composite for boosting microwave attenuation performance in 2-18 GHz. *Carbon* **2022**, *193*, 182–194. [[CrossRef](#)]
40. Bao, Y.; Guo, S.; Wang, W.; Qi, X.; Jia, Z.; Guan, H. Heterogeneous burr-like CoNiO₂/Ti₃C₂T_x MXene nanospheres for ultralow microwave absorption and satellite skin application. *Chem. Eng. J.* **2023**, *473*, 145409. [[CrossRef](#)]
41. Li, C.; Qi, X.S.; Gong, X.; Peng, Q.; Chen, Y.L.; Xie, R.; Zhong, W. Magnetic-dielectric synergy and interfacial engineering to design yolk-shell structured CoNi@void@C and CoNi@void@C@MoS₂ nanocomposites with tunable and strong wideband microwave absorption. *Nano Res.* **2022**, *15*, 6761–6771. [[CrossRef](#)]
42. Ni, C.; Wu, D.; Xie, X.B.; Wang, B.L.; Wei, H.L.; Zhang, Y.; Zhao, X.J.; Liu, L.; Wang, B.; Du, W. Microwave absorption properties of microporous CoNi@(NiO-CoO) nanoparticles through dealloying. *J. Magn. Magn. Mater.* **2020**, *503*, 166631. [[CrossRef](#)]
43. Guo, Z.Z.; Ren, P.G.; Yang, F.; Wu, T.; Zhang, L.X.; Chen, Z.Y.; Huang, S.Q.; Ren, F. MOF-Derived Co/C and MXene co-Decorated Cellulose-Derived Hybrid Carbon Aerogel with a Multi-Interface Architecture toward Absorption-Dominated Ultra-Efficient Electromagnetic Interference Shielding. *ACS Appl. Mater. Interfaces* **2023**, *15*, 7308–7318. [[CrossRef](#)] [[PubMed](#)]
44. Chen, F.; Zhang, S.S.; Ma, B.B.; Xiong, Y.; Luo, H.; Cheng, Y.Z.; Li, X.C.; Wang, X.; Gong, R.Z. Bimetallic CoFe-MOF@Ti₃C₂T_x MXene derived composites for broadband microwave absorption. *Chem. Eng. J.* **2022**, *431*, 134007. [[CrossRef](#)]
45. Cai, L.; Pan, F.; Zhu, X.J.; Dong, Y.Y.; Shi, Y.Y.; Xiang, Z.; Cheng, J.; Jiang, H.J.; Shi, Z.; Lu, W. Etching engineering and electrostatic self-assembly of N-doped MXene/hollow Co-ZIF hybrids for high-performance microwave absorbers. *Chem. Eng. J.* **2022**, *434*, 133865. [[CrossRef](#)]
46. Hu, F.Y.; Wang, X.H.; Niu, H.H.; Zhang, S.; Fan, B.B.; Zhang, R. Synthesis and electromagnetic wave absorption of novel Mo₂TiC₂T_x MXene with diverse etching methods. *J. Mater. Sci.* **2022**, *57*, 7849–7862. [[CrossRef](#)]
47. Zhu, S.Q.; Gao, Y.; Zhou, H.R.; Zheng, C.L.; Li, X.B.; Man, Q.K.; Liu, X.C. Expanded graphite/Co@C composites with dual functions of corrosion resistance and microwave absorption. *J. Mater. Res. Technol.* **2023**, *23*, 3557–3569. [[CrossRef](#)]
48. Wu, M.; Wang, H.C.; Liang, X.H.; Wang, D.H. Flower-like 1T/2H-MoS₂@α-Fe₂O₃ with enhanced electromagnetic wave absorption capabilities in the low frequency range. *J. Mater. Chem. C* **2023**, *11*, 2897–2910. [[CrossRef](#)]
49. Wu, Q.; Wang, B.L.; Fu, Y.G.; Zhang, Z.F.; Yan, P.F.; Liu, T. MOF-derived Co/CoO particles prepared by low temperature reduction for microwave absorption. *Chem. Eng. J.* **2021**, *410*, 128378. [[CrossRef](#)]
50. Jia, Z.R.; Zhang, X.Y.; Gu, Z.; Wu, G.L. MOF-derived Ni-Co bimetal/porous carbon composites as electromagnetic wave absorber. *Adv. Compos. Hybrid Mater.* **2023**, *6*, 28. [[CrossRef](#)]
51. Jiang, B.; Yang, W.; Wang, C.N.; Bai, H.X.; Ma, G.; Li, Z.X.; Zhang, C.X.; Li, S.Y.; Chen, N.; Ta, N.; et al. Lightweight porous cobalt-encapsulated Nitrogen-Doped Carbon nanotubes for tunable, efficient and stable electromagnetic waves absorption. *Carbon* **2023**, *202*, 173–186. [[CrossRef](#)]
52. Yang, K.; Cui, Y.H.; Wan, L.Y.; Wang, Y.B.; Tariq, M.R.; Liu, P.; Zhang, Q.Y.; Zhang, B.L. Preparation of three-dimensional Mo₂C/NC@MXene and its efficient electromagnetic absorption properties. *ACS Appl. Mater. Interfaces* **2022**, *14*, 7109–7120. [[CrossRef](#)] [[PubMed](#)]
53. Lu, Z.X.; Ren, F.; Guo, Z.Z.; Dai, Z.; Fu, B.Q.; Zong, Z.; Zhang, F.D.; Jin, Y.L.; Chen, Z.Y.; Ren, P.G. Facile construction of core-shell Carbon@CoNiO₂ derived from yeast for broadband and high-efficiency microwave absorption. *J. Colloid Interface Sci.* **2022**, *625*, 415–424. [[CrossRef](#)] [[PubMed](#)]
54. Li, X.; Wu, Z.C.; You, W.B.; Yang, L.T.; Che, R.C. Self-assembly MXene-rGO/CoNi film with massive continuous heterointerfaces and enhanced magnetic coupling for superior microwave absorber. *Nano-Micro Lett.* **2022**, *14*, 73. [[CrossRef](#)] [[PubMed](#)]
55. Sun, Q.; Yang, X.; Shu, T.; Yang, X.F.; Qiao, M.; Wang, D.S.; Liu, Z.H.; Li, X.H.; Rao, J.S.; Zhang, Y.X.; et al. In situ synthesis of C-N@NiFe₂O₄@MXene/Ni nanocomposites for efficient electromagnetic wave absorption at an ultralow thickness level. *Molecules* **2023**, *28*, 233. [[CrossRef](#)] [[PubMed](#)]
56. Yang, J.J.; Wang, J.Q.; Li, H.Q.; Wu, Z.; Xing, Y.Q.; Chen, Y.F.; Liu, L. MoS₂/MXene aerogel with conformal heterogeneous interfaces tailored by atomic layer deposition for tunable microwave absorption. *Adv. Sci.* **2022**, *9*, 2101988. [[CrossRef](#)] [[PubMed](#)]
57. Zhi, D.D.; Li, T.; Qi, Z.H.; Li, J.Z.; Tian, Y.R.; Deng, W.T.; Meng, F.B. Core-shell heterogeneous graphene-based aerogel microspheres for high-performance broadband microwave absorption via resonance loss and sequential attenuation. *Chem. Eng. J.* **2022**, *433*, 134496. [[CrossRef](#)]
58. Zhou, C.G.; Wang, X.X.; Luo, H.; Deng, L.W.; Wei, S.; Zheng, Y.W.; Jia, Q.; Liu, J.Q. Rapid and direct growth of bipyramid TiO₂ from Ti₃C₂T_x MXene to prepare Ni/TiO₂/C heterogeneous composites for high-performance microwave absorption. *Chem. Eng. J.* **2020**, *383*, 123095. [[CrossRef](#)]
59. Zhang, C.; Wu, Z.C.; Xu, C.Y.; Yang, B.T.; Wang, L.; You, W.B.; Che, R.C. Hierarchical Ti₃C₂T_x MXene/carbon nanotubes hollow microsphere with confined magnetic nanospheres for broadband microwave absorption. *Small* **2022**, *18*, 2104380. [[CrossRef](#)]

60. Liang, G.Y.; Han, F.; Ye, X.Y.; Meng, X.F. Hierarchical 0D/2D NiFe₂O₄/Ti₃C₂T_x MXene composites for boosting microwave absorption. *Mater. Sci. Eng. B-Adv.* **2023**, *289*, 116224. [[CrossRef](#)]
61. Ni, Q.Q.; Zhu, Y.F.; Yu, L.J.; Fu, Y.Q. One-dimensional carbon nanotube@barium titanate@polyaniline multiheterostructures for microwave absorbing application. *Nanoscale Res. Lett.* **2015**, *10*, 174. [[CrossRef](#)] [[PubMed](#)]
62. Bai, Y.H.; Zhang, D.Y.; Lu, Y. Foamed concrete composites: Foamed concrete composites: Mn–Zn ferrite/carbon fiber synergy enhances electromagnetic wave absorption performance. *Ceram. Int.* **2023**, *49*, 33703–33716. [[CrossRef](#)]
63. Guo, T.; Huang, B.; Li, C.G.; Lou, Y.M.; Tang, X.Z.; Huang, X.Z.; Yue, J.L. Magnetic sputtering of FeNi/C bilayer film on SiC fibers for effective microwave absorption in the low-frequency region. *Ceram. Int.* **2021**, *47*, 5221–5226. [[CrossRef](#)]
64. Song, Y.; Zheng, J.; Liu, X.J.; Sun, M.; Zhao, S. Facile synthesis of BaTiO₃ on multiwalled carbon nanotubes as a synergistic microwave absorber. *J. Mater. Sci.-Mater. Electron.* **2016**, *27*, 3390–3396. [[CrossRef](#)]
65. Liao, Q.; He, M.; Zhou, Y.M.; Nie, S.X.; Wang, Y.J.; Hu, S.C.; Yang, H.Y.; Li, H.F.; Tong, Y. Highly cuboid-shaped heterobimetallic metal-organic frameworks derived from porous Co/ZnO/C microrods with improved electromagnetic wave absorption capabilities. *ACS Appl. Mater. Interfaces* **2018**, *10*, 29136–29144. [[CrossRef](#)]
66. Du, B.Y.; Chai, L.F.; Li, W.; Wang, X.; Chen, X.H.; Zhou, J.H.; Sun, R.C. Preparation of functionalized magnetic graphene oxide/lignin composite nanoparticles for adsorption of heavy metal ions and reuse as electromagnetic wave absorbers. *Sep. Purif. Technol.* **2022**, *297*, 121509. [[CrossRef](#)]

Disclaimer/Publisher’s Note: The statements, opinions and data contained in all publications are solely those of the individual author(s) and contributor(s) and not of MDPI and/or the editor(s). MDPI and/or the editor(s) disclaim responsibility for any injury to people or property resulting from any ideas, methods, instructions or products referred to in the content.